Strong, ductile, and hierarchical hetero-lamellar-structured alloys through microstructural inheritance and refinement

Shi, Peijian; Li, Yi; Li, Zhi; Jiang, Xin; Yan, Jie; Zhou, Rui; Qin, Yi; Lin, Yifan; Huang, Jingran; Tan, Bodong; Wang, Yinan; Wen, Tongqi; Ye, Beilin; Ling, Chunyan; Luan, Junhua; Shen, Zhe; Ding, Biao; Li, Qiang; Zheng, Tianxiang; Ren, Weili; Zhang, Tianlong; Ren, Yang; Zhong, Yunbo; Liu, C. T.; Gao, Huajian; Zhu, Yuntian

Published in:
Proceedings of the National Academy of Sciences of the United States of America

Published: 14/01/2025

Document Version:
Final Published version, also known as Publisher's PDF, Publisher's Final version or Version of Record

Published version (DOI):
10.1073/pnas.2409317121

Publication details:
Shi, P., Li, Y., Li, Z., Jiang, X., Yan, J., Zhou, R., Qin, Y., Lin, Y., Huang, J., Tan, B., Wang, Y., Wen, T., Ye, B., Ling, C., Luan, J., Shen, Z., Ding, B., Li, Q., Zheng, T., ... Zhu, Y. (2025). Strong, ductile, and hierarchical hetero-lamellar-structured alloys through microstructural inheritance and refinement. *Proceedings of the National Academy of Sciences of the United States of America*, *122*(2), Article e2409317121. https://doi.org/10.1073/pnas.2409317121

PNAS RESEARCH ARTICLE | ENGINEERING OPEN ACCESS

Strong, ductile, and hierarchical hetero-lamellar-structured alloys through microstructural inheritance and refinement

Peijian Shi[a,b,1,2], Yi Li[a,1], Zhi Li[c,1], Xin Jiang[a], Jie Yan[b], Rui Zhou[b], Yi Qin[a], Yifan Lin[a], Jingran Huang[a], Bodong Tan[a], Yinan Wang[d,e], Tongqi Wen[f], Beilin Ye[f], Chunyan Ling[g], Junhua Luan[b], Zhe Shen[a], Biao Ding[a], Qiang Li[a], Tianxiang Zheng[a], Weili Ren[a], Tianlong Zhang[h], Yang Ren[i], Yunbo Zhong[a,2], C. T. Liu[b,2], Huajian Gao[j,2], and Yuntian Zhu[b,2]

Affiliations are included on p. 12.

Edited by Peter K. Liaw, The University of Tennessee Knoxville, Knoxville, TN; received May 12, 2024; accepted November 20, 2024 by Editorial Board Member John A. Rogers

The strength–ductility trade-off exists ubiquitously, especially in brittle intermetallic-containing multiple principal element alloys (MPEAs), where the intermetallic phases often induce premature failure leading to severe ductility reduction. Hierarchical heterogeneities represent a promising microstructural solution to achieve simultaneous strength–ductility enhancement. However, it remains fundamentally challenging to tailor hierarchical heterostructures using conventional methods, which often rely on costly and time-consuming processing. Here, we report a multiscale microstructural inheritance and refinement strategy to process "structural hierarchy precursors" in as-cast heterogeneous $Al_{0.7}$CoCrFeNi MPEAs, which lead directly to a hierarchical hetero-lamellar structure (HLS) after simple rolling and annealing. Interestingly, it takes only 10 min of annealing time, two orders of magnitude less than that required to render the state-of-the-art properties during conventional processing of $Al_{0.7}$CoCrFeNi, for us to achieve record-high strength–ductility combinations via the hierarchical HLS design that sequentially stimulates multiple unusual deformation and reinforcement mechanisms. In particular, the HLS-enabled high hetero-deformation-induced (HDI) internal stress triggers profuse <111>-type dislocations on over five independent slip systems in the supposedly brittle intermetallic phase and activates extensive stacking faults (SFs) and nanotwinning in the adjoining soft phase with a rather high SF energy. These unexpected, dynamically reinforcing hetero-deformation mechanisms across multiple length scales facilitate high sustained HDI strain hardening, along with a salient microcrack-mediated extrinsic ductilization effect, suggesting that the proposed microstructural inheritance and refinement strategy provides an efficient, fast, and low-cost approach to overcome the strength–ductility trade-off in a broad range of structural materials.

high-entropy alloy | hierarchical hetero-lamellar structure | strong HDI stress | multiple previously inaccessible micromechanisms | superior strength–ductility synergy

Significance

Brittle intermetallic phases that exist ubiquitously in diverse technologically important structural materials, especially in multiple principal element alloys, hamper practical applications due to premature failure. Here, we report a hierarchical hetero-lamellar structure (HLS) fabricated using a microstructural inheritance and refinement strategy that involves simple rolling followed by rapid annealing in a brittle B2-intermetallic-containing $Al_{0.7}$CoCrFeNi MPEA. By harnessing high hetero-deformation-induced internal stresses, the designed HLS sequentially stimulates multiple previously inaccessible deformation and reinforcement mechanisms, which not only ductilize the brittle B2 phase, preempting premature failure, but also substantially strain-harden the adjoining soft phase to sustain stable tensile flow, leading to superior strength–ductility enhancement. This fast and low-cost microstructural design strategy is expected to impact a broad range of structural materials.

Multiple principal element alloys (MPEAs), also dubbed as high-entropy alloys, have rendered vast opportunities in seeking optimal mechanical performance of materials within a seemingly infinite compositional space (1–6). Despite these merits, their superior properties often overly depend on complex thermomechanical processing of lengthy high-temperature homogenization annealing (e.g., at 1,200 °C for 24 h), costly hot forging/rolling, as well as further cold-rolling and annealing treatments (7–9). In addition, the strength of many previous single-phase MPEAs, especially yield strength (typically <500 MPa), is generally insufficient for many practical applications, although their ductility is surplus (7–9). To this end, certain strategies that involve the introduction of extensive phase boundaries have been widely adopted to increase the yield strength of MPEAs (10–13). However, a consequence is that their tensile ductility often becomes rather limited, even less than a few percent, due to the frequent introduction of hard brittle intermetallic phases (readily triggering premature failure) (12, 13). Recently, hierarchical heterogeneities have showcased a promising microstructural solution to overcome the prevailing strength–ductility trade-off (3, 14–16). However, it remains a fundamental challenge to tailor hierarchical hetero-structures at multiple length scales, particularly in bulk alloy materials, at low cost.

Facing these dilemmas, we note that in many as-cast MPEAs, their dual/multiphase components generally span several length scales, as well as feature spatially varying distributions and hardness differences; these natural traits, therefore, can function as simple and elementary hierarchical hetero-structures (14–16). Such hetero-phase-assembled multiscale structural precursors, together with thermo-mechanically processed phase refinement, potentially allow in situ access to desired hierarchical heterogeneity designs with great processing simplification.

[1]P.S., Y.L., and Z.L. contributed equally to this work.

[2]To whom correspondence may be addressed. Email: shipeijian11@gmail.com, yunboz@staff.shu.edu.cn, chainliu@cityu.edu.hk, gao.huajian@tsinghua.edu.cn, or y.zhu@cityu.edu.hk.

This article contains supporting information online at https://www.pnas.org/lookup/suppl/doi:10.1073/pnas.2409317121/-/DCSupplemental.

Published January 8, 2025.

Taking this clue, we report a microstructural inheritance and refinement coupled design strategy. Through simple cold rolling and one-step annealing, this strategy has been demonstrated in a triple-phase-composed multiscale hetero-lamellar $Al_{0.7}$CoCrFeNi (at.%) MPEA (17–20). Specifically, during thermomechanical processing, we carefully control the hetero-lamellar-hierarchy precursor of as-cast $Al_{0.7}$CoCrFeNi to be progressively deformed, elongated, and aligned, rather than completely destroying them as in previous processing methods. Along with the concurrent introduction of a large number of finer micro- to nanoscale substructures, we established a heredity-derived and -refined hierarchical hetero-lamellar structure (HLS) with synergistic phase and chemical modulations across multiple length scales.

The hierarchical HLS not only significantly elevates the yield strength but also sequentially activates multiple unusual deformation and reinforcement mechanisms concomitant with widespread, diversified dislocation gliding and trapping. In particular, the HLS enables intense hetero-deformation-induced (HDI) stresses, which stimulate massive <111>-type dislocations in an intrinsically brittle B2 intermetallic phase. Compared to previously observed <100> ones, these <111> dislocations, containing over 5 independent slip systems (ISSs), hence allow extensile plastic flow, leading to salient intermetallic ductilization. Moreover, strong HDI stresses trigger profuse stacking faults (SFs) and nanotwinning even in unfavorable grains with a high SF energy of ~3 mJ/m^2, far above the energy regime for twinning. Thus, a sustained high HDI strain hardening and even hierarchical crack buffering effect are equipped. These collectively promote exceptionally robust strength–ductility combinations, not accessible to any previous reinforcement methodologies in the $Al_{0.7}$CoCrFeNi MPEAs (18–20).

Of particular emphasis here is that previous $Al_{0.7}$CoCrFeNi systems (18–20) have never reached strength–ductility combinations on par with the best in other reported high figure-of-merit MPEA categories, as the former contain dense brittle B2 intermetallic (prone to premature failure) and cannot initiate deformation twins to markedly enhance tensile properties (yet frequently observed in the latter) (6–9). These cases severely limit tensile properties of the studied $Al_{0.7}$CoCrFeNi. However, our property profiles achieved without changing chemical composition are comparable to those of previous advanced MPEA species. These compelling facts again indicate the feasibility and high efficiency of our microstructural inheritance and refinement strategy, particularly in terms of property enhancements.

Apart from delivering superior properties, our inheritance and refinement coupled strategy greatly simplifies the processing procedure, only remaining simple cold rolling and one-step annealing. Previously, to seek for optimal performance, this prototype MPEA needs to undergo lengthy, costly, and multistep thermo-mechanical processing (18). In contrast, our design strategy substantially relieves these complicated treatments. In particular, our total annealing time has been shortened to just 10 min, approximately two orders of magnitude less than the state of the art in the $Al_{0.7}$CoCrFeNi (18), which, however, promotes better strength–ductility combinations. In a nutshell, our demonstrated rapid, economic multiscale inheritance and refinement strategy, capable of extreme property enhancement, has broad implications for the development of hierarchical, hetero-structured, dual-/multiphase strong-yet-ductile bulk materials at low cost and large scale.

As-Cast Hetero-Lamellar-Hierarchy Precursor

Fig. 1*A* shows electron backscattered diffraction (EBSD) phase map and inverse pole figure (IPF). The joint EBSD characterizations combined with scanning electron microscopy (SEM) images (*SI Appendix*, Fig. S1) reveal that the as-cast $Al_{0.7}$CoCrFeNi MPEA possesses a near-equiaxed nondendritic grain structure with an average size of ~280 μm. Such as-cast grains are composed of face-centered cubic (FCC) and body-centered cubic (BCC) dual phases with a FCC-phase content of ~65 vol.%. Specifically, the as-cast grains comprise a grain-boundary (allotriomorphic) FCC film phase and intragranular (idiomorphic) FCC and BCC mixed phases (Fig. 1*A* and *SI Appendix*, Fig. S1). The intragranular region contains a predominant Widmanstätten-like lamellar structure (~94 vol.%) and sporadic vermicular structure, as confirmed by Fig. 1 *A* and *B* and *SI Appendix*, Fig. S2. The gray side and black interside lamellae in Fig. 1*B* are FCC and BCC phases, respectively. Note that these dual-phase lamellae exhibit broadly varied thicknesses and lengths, spanning from submicrons to over 100 μm, as revealed in Fig. 1*A* and quantified in *SI Appendix*, Fig. S3. In addition, due to different variant selections, these lamellae form different intragranular colonies with varied growth directions (Fig. 1*A* and *SI Appendix*, Fig. S1). To provide more structural details, we conducted nanometer-resolved transmission electron microscopy (TEM) investigations. We confirm the side FCC lamellae to be devoid of precipitates (*SI Appendix*, Fig. S4), while the interside lamellae exhibit a finer basket-weave-like modulating substructure (Fig. 1 *C*, *Upper*). Corresponding selected-area electron diffractions (SAEDs; Fig. 1*C*, under) reveal that the modulating substructure is composed of near-nanometer-thick disordered BCC and ordered B2 two phases, rather than the EBSD-identified single BCC phase due to its limited resolution.

Thus, without resorting to any additional processing, the directly solidified $Al_{0.7}$CoCrFeNi MPEA exhibits a triple-phase-assembled hierarchical lamellar heterogeneity across multiple length scales. We show that the as-cast hierarchical heterostructure, which derives from a negative mixing enthalpy (−10.57 kJ/mol) of $Al_{0.7}$CoCrFeNi (21, 22), is a result of nonequilibrium solidification from the liquid to a single metastable B2 phase, followed by spontaneous two-step solid-state phase decomposition upon cooling. The two-step decomposition involves the allotropic transformation of the metastable B2 phase → FCC phase and the spinodal decomposition of the rest B2 phase → new B2 + BCC phases (17), as indicated by thermodynamic modeling in *SI Appendix*, Fig. S5 *A* and *B* and schematically illustrated in *SI Appendix*, Fig. S5*C*. Among them, the FCC phase nucleates preferentially at high-energy grain boundaries as allotriomorphs, followed by the growth of colonies of FCC lamellae into the B2 grain in a Widmanstatten-like fashion. This phenomenon occurs because the nucleation barrier is higher for the direct formation of other hybrid phases in the B2-matrix grain (17–19). Thus, some aspects of the above solid-state transformation resemble the colony-like microstructure observed in the case of α/β Ti alloys (23–25), but without undergoing spinodal decomposition as in our studied MPEA. Overall, our directly solidified hierarchical hetero-lamellar MPEAs show significant uniqueness, and more solidification and phase-decomposition details are provided in *SI Appendix*, *Note S1*.

As-Processed Hierarchical HLS

Fig. 1 *D*–*K* shows the as-processed hierarchical HLS in the $Al_{0.7}$CoCrFeNi MPEA. To achieve the exquisite hierarchical heterostructure, we deliberately explore multiscale microstructural inheritance and refinement for the as-cast hetero-lamellar-hierarchy precursor (Fig. 1 *A*–*C*) through carefully controlling cold-rolling and annealing treatments, rather than completely breaking them as in conventional processing paradigms. Specifically, during optimized thermomechanical processing, the multiscale inheritance is evolved by the progressive plastic deformation, alignment, and

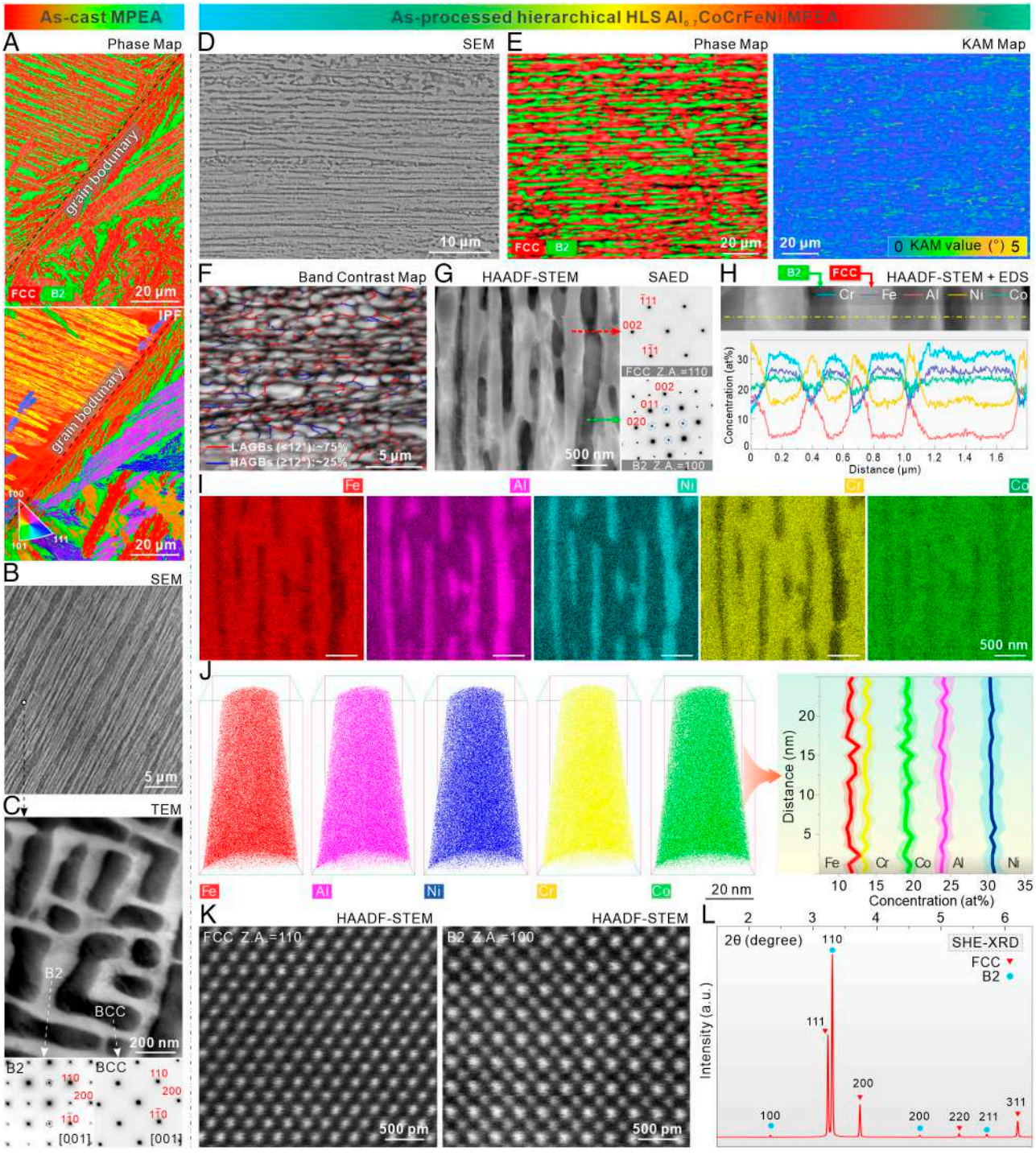

Fig. 1. Heredity-derived and -refined hierarchical HLS MPEAs. (*A*–*C*) As-cast lamellar structure revealed by EBSD phase map and IPF (*A*), SEM image (*B*), and TEM image and SAED patterns (*C*). (*D*–*L*) As-processed hierarchical HLS shown by SEM image (*D*), EBSD phase map and KAM image (*E*), band contrast map overlapped with LAGBs and HAGBs (*F*), HAADF-STEM image and SAED patterns (*G*), HAADF-STEM image and EDS line scanning (*H*), EDS element mapping (*I*), 3D APT map and associated line scanning of five elements (*J*), atomic-scale HAADF-STEM images of FCC and B2 phases (*K*), and SHE-XRD image (*L*).

elongation of as-cast hierarchical hetero-lamellae along the rolling direction (RD), as well as the concurrent refinement along the thickness direction (TD) of the rolled samples. Thus, the as-cast hetero-lamellar hierarchy successfully functions as an effective structural precursor–making the heredity-derived and refined $Al_{0.7}$CoCrFeNi MPEA correspondingly exhibit a 3D hierarchical heterostructure with broadly varied lamellar length, thickness, continuity, and topology distribution (Fig. 1 *D*–*I*). More fundamental heredity-derived and refined details operating at multi-length scales are as follows.

These as-cast lamellae with an angle of <60° to the RD can be gradually aligned and elongated along the RD during the rolling deformation (Fig. 1 *D* and *E* and *SI Appendix*, Fig. S6). Among them, these lamellae parallel to the RD will undergo significant and direct elongation along the RD. These lamellae that are not parallel to the RD need additional alignment processes potentially coming with varying degrees of the lamellar thickening, resulting in relatively short lamellar elongation. As such, the diversified deformation trends allow for further changes in both lamellar thickness and length, which, together with potential substructure introduction and phase

refinement along the TD, can promote the desired hierarchical-lamellar-heterogeneity design. Meanwhile, there should be a few regions, e.g., (near-) vertical lamellar colonies relative to the RD, which cannot be aligned successfully during the rolling process, thus forming a small proportion of weak or broken lamellar regions (*SI Appendix*, Fig. S6). Overall, thanks to highly developed lamellar precursors in the as-cast condition, the as-processed $Al_{0.7}$CoCrFeNi MPEA displays exceptionally profuse lamellar nature (Fig. 1 *D*–*I*). In turn, the profuse lamellar nature delivers direct evidence underlying our proposed microstructure-inheritance design strategy.

Further considering the statistical distribution of the initial as-cast lamellar size and direction, these above deformation scenarios hence promote the observed hierarchical hetero-structure characterized by broadly varied length, thickness, continuity, and topology distribution in terms of these inherited lamellae (Fig. 1 *D*–*I* and *SI Appendix*, Fig. S6). In addition, it was revealed that these inherited lamellae contain abundant high-angle grain boundaries (HAGBs) and low-angle grain boundaries (LAGBs), especially the latter with small spacing of ~3.42 μm and ultrahigh proportion of ~75% (Fig. 1*F*). Such profuse substructures, therefore, demonstrate a concurrent, considerable microstructure refinement in the inherited lamellae, which, together with the lamellar refinement along the TD, greatly enriches and diversifies the desired hierarchical hetero-lamellar architecture (Fig. 1 *D*–*I* and *SI Appendix*, Fig. S6).

Rapid, Economic Processing Route

Behind the heredity-derived and -refined hierarchical HLS design, it should be stressed that our processing strategy is rather simple, only involving cold rolling and annealing, especially the latter taking just 10 min at 1,000 °C, as schematically illustrated in Fig. 2*A*. The applied annealing time is much shorter than those reported cases in the $Al_{0.7}$CoCrFeNi MPEA (18–20). In addition, the joint SAED pattern and atomic-scale high-angle annular dark field (HAADF) scanning TEM (STEM) probing (Fig. 1 *G* and *K*) revealed that the present annealing parameter allows the rapid dissolution of the spinodally decomposed BCC phase into the B2 matrix, and no other phases are formed in adjacent FCC lamellae. We further conducted three-dimensional atom probe tomography (3D-APT) analyses (Fig. 1*J*), revealing that the B2 phase has a homogeneous NiAl-rich chemical composition of 31.56 ± 1.41 at.% Ni, 24.27 ± 1.18 at.% Al, 18.61 ± 1.11 at.% Co, 11.60 ± 0.87 at.% Fe, and 13.96 ± 0.92 at.% Cr, without containing element clustering or segregation. Additional EDS line scanning and element mapping (Fig. 1 *H* and *I*) also confirm the NiAl-rich B2 phase, as well as reveal that the FCC phase has a FeCr-rich composition of 15.26 ± 1.04 at.% Ni, 4.22 ± 0.84 at.% Al, 23.15 ± 1.64 at.% Co, 26.14 ± 1.15 at.% Fe, and 31.23 ± 1.54 at.% Cr. Finally, to compensate for the limited sampling area/volume of TEM and 3D-APT, we performed synchrotron high-energy X-ray diffraction (SHE-XRD; Fig. 1*L*), confirming that our bulk hierarchical HLS MPEAs indeed only contain two phases, FCC and B2, without detecting other new phases.

Such dual-phase components observed here are obviously different from those reported cases (18, 19). In the reported latter, introducing additional phases, i.e., dense nanoprecipitates, in both the FCC and B2 phases has been shown to be an optimal strategy for achieving the best strength–ductility combinations among $Al_{0.7}$CoCrFeNi MPEAs (18). But to achieve them, complex multistep thermomechanical treatments are required, as schematically illustrated in Fig. 2*B*. Specifically, the as-cast MPEAs first need to be homogenized at 1,150 °C for 1 h or higher temperature and longer time to reduce microsegregations from the casting process as well as to prevent cracking in subsequent cold/hot rolling. Then, further annealing at a high temperature (~1,000 °C) was conducted to homogenize and recrystallize severely deformed samples. Finally, for the homogenized and recrystallized samples, a much long annealing period, up to 24 h, at a medium temperature (580 °C) is required for full aging, so as to maximize dual precipitation strengthening in both the FCC and B2 phases. Thus, as marked by green squares in Fig. 2 *C* and *D*, the resulting homogeneous-structured, precipitation-strengthened (HSPS) $Al_{0.7}$CoCrFeNi MPEA exhibits the state-of-the-art property combination among those reported findings.

Extreme Strength–Ductility Enhancement

As shown in Fig. 2 *A* and *B*, our total heat-treatment time (only 10 min) is two orders of magnitude less than that of the reported state-of-the-art HSPS finding. But surprisingly, our hierarchical HLS $Al_{0.7}$CoCrFeNi MPEA exhibits a gigapascal-level yield strength of 1,072 ± 22 MPa and commendable tensile ductility with a uniform elongation up to 20.5 ± 1.2% (see red curve; Fig. 2*E*). Such an appreciable strength–ductility combination, as revealed in Fig. 2 *C* and *D*, is significantly superior to the reported state-of-the-art property level (ref. 18). In particular, compared to the latter, our uniform elongation increases by ~71% without sacrificing any yield strength. In addition, a more remarkable strength–ductility enhancement can be identified relative to their as-cast counterparts (see red and black curves, respectively; Fig. 2*E*), where the yield strength is elevated to approximately 2 times, while the uniform elongation is more markedly increased to more than 4 times.

To more directly demonstrate the extreme strength–ductility enhancement, we compare our tensile properties with those of not only high-strength $Al_{0.7}$CoCrFeNi MPEAs but also their massive derived and similar alloy systems to date (Fig. 2 *C* and *D* and *SI Appendix*, Table S1). As shown, our hierarchical HLS-reinforced MPEAs (see red pentagrams) successfully evade the prevailing strength–ductility trade-off dilemma in $Al_{0.7}$CoCrFeNi MPEAs and exhibit salient property combinations, which make them clearly stand out among those reported property profiles in Fig. 2 *C* and *D*.

Also note that these impressive properties are highly competitive, and some of them are even superior, to many reported excellent ones in other high figure-of-merit MPEA systems (26–29). However, those previous property results in $Al_{0.7}$CoCrFeNi MPEAs (*SI Appendix*, Table S1) have never reached strength–ductility combinations on par with the best in other advanced MPEA categories, as the former contain dense brittle B2 intermetallic (prone to premature failure) and cannot initiate deformation twins and/or phase transformations to markedly enhance tensile properties (yet frequently observed in the latter) (6–9). These incidents severely limit tensile properties of the studied $Al_{0.7}$CoCrFeNi. Thus, our current record-breaking property trend again indicates the feasibility and high efficiency of our microstructural inheritance and refinement strategy in respect to performance enhancements.

Strain-Hardening Mechanisms

After achieving these attractive properties and attributes, it naturally follows to investigate their underlying strengthening and strain-hardening mechanisms. By comparing with those previously reported findings (18–20), we show that the high, gigapascal-level yield strength can be ascribed to grain-boundary strengthening (i.e., lamellar refinement), as revealed by EBSD observations (Fig. 1 *E* and *F*) and *SI Appendix*, *Note S2*. In addition, due to the inherited profuse hetero-lamellar nature, our hierarchical HLS MPEAs exhibit a high HDI stress up to ~610 MPa, i.e., salient HDI strengthening (to be detailed later).

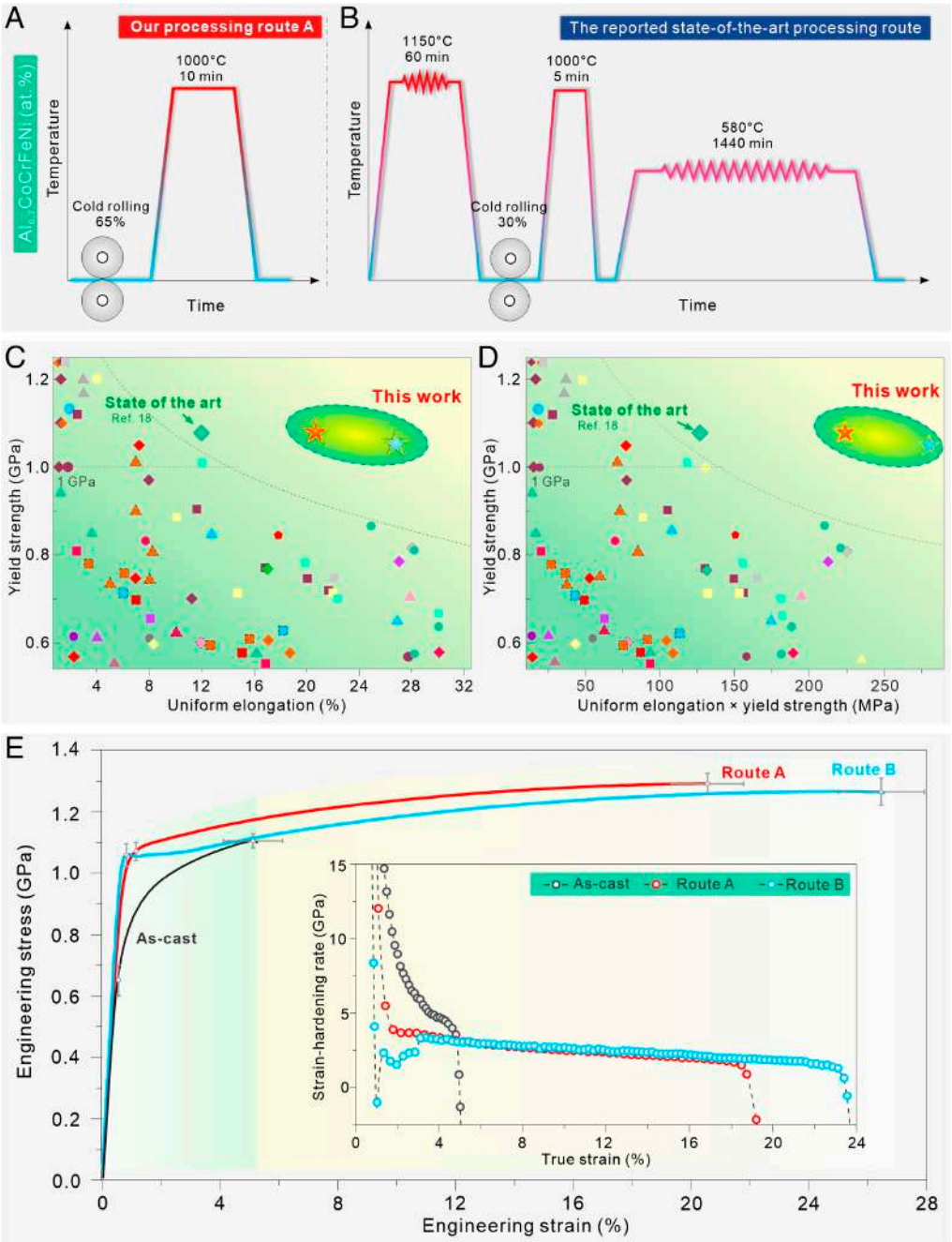

Fig. 2. Rapid, facile thermomechanical processing rendering superior tensile properties. (*A*) Our processing route A. Our processing route B is provided in *SI Appendix*, Fig. S13. (*B*) Reported lengthy, costly, and complex processing route. (*C* and *D*) Comparison of tensile properties of (*C*) yield strength versus uniform elongation and (*D*) the product of yield strength and uniform elongation versus yield strength compared with all $Al_{0.7}$CoCrFeNi MPEAs as well as their similar and derived alloy systems. Two bigger green squares (marked by green arrows in *C* and *D*) illustrate the reported best property combinations before our work. All property data refer to *SI Appendix*, Table S1. (*E*) Tensile curves of one as-cast and two as-processed $Al_{0.7}$CoCrFeNi MPEAs. The *Inset* shows the associated three strain-hardening curves.

Severe Intrinsic Brittleness. Before unveiling the excellent ductility, we first provide some essential discussion about the commonly found brittle problem of the B2 intermetallic phase in the $Al_{0.7}$CoCrFeNi MPEA, which often triggers premature failure leading to inferior ductility (20). Actually, such a brittle problem is increasingly observed in many other dual/multiphase MPEAs, such as eutectic MPEAs (3, 10, 11). It has been reported that these B2 intermetallic phases with NiAl-rich chemical compositions usually have high anti-phase boundary energies (450 to 885 mJ/m^2), which cause limited available slip systems of dislocations during tensile deformation (30), thus rendering severe intrinsic brittleness. Specifically, the available dislocations of these B2 intermetallic phases are often governed by {110}<100> with only three ISSs, whereas for generalized polycrystalline deformation, at least five ISSs are required according to the von Mises criterion (30). Unfortunately, activation of dislocations with higher ISSs at room temperature requires huge critical stresses, which make it difficult to activate these efficient dislocations to sustain plastic deformation, thereby leading to premature material failure.

These above dilemmas also exist in our studied as-cast $Al_{0.7}$CoCrFeNi MEAs, whereby the actual fractography examination after tension identifies a distinct cleavage fracture on the B2/BCC phases (Fig. 3 *I* and *J*). In terms of deformation mechanisms, it was revealed that these soft FCC lamellae with large angles (30 to 60°) to the tensile loading direction (TLD) generally undergo weak deformation constraint by adjacent hard brittle B2/BCC phases, thus experiencing the initial plastic deformation (Fig. 3 *A* and *B*) operating with profuse slip lines and interactions (see *Inset*, Fig. 3*B*). However, this preferential deformation tends to cause incompatible intragranular and/or intergranular deformation with some neighboring colonies and/or grains, respectively, when the latter exhibit high strength due to their lamellar directions with minor angles to the TLD, for example. With increasing tensile strains, serious stress concentrations inevitably occur between these easily deformable and nondeformable lamellae, as manifested by

widespread concave and convex undulations on the prepolished specimen surface (Fig. 3 *C* and *D*). Consequently, cracks are frequently observed in these colonies around their boundaries (marked by red arrows; Fig. 3*D* and *SI Appendix*, Fig. S7), which triggered premature failure with much low as-cast ductility (~5%; Fig. 2*E*). Besides, the inferior as-cast ductility can be further ascribed to the B2 intermetallic phase, which features extremely intrinsic brittleness and offers very limited tensile ductility. This general fact, in turn, rationalizes that in those reported findings (18–20), the brittle problem of the B2 intermetallic has not been fully resolved, thereby leading to relatively limited ductility improvement, as exemplified by the massive experimental data in Fig. 2*C*.

In view of these dilemmas existing broadly in both as-cast and those reported conditions, we believe that our well-aligned, hierarchical, and partially recrystallized HLS can activate extensive plastic deformation of the B2 phase in the $Al_{0.7}CoCrFeNi$, as evidenced by its ductile fracture in Fig. 3 *K* and *L*. Such deformation scenarios hence prevent premature intragranular/intergranular cracking, leading to the observed excellent ductility (Fig. 2*E*). Although there are some adjacent regions with varying lamellar directions (Fig. 3*F*), we did not observe severe incompatible deformation seen in their as-cast counterparts. This improved deformation behavior can be ascribed to the relatively smaller angle differences (<30°) between adjoining lamellar regions due to the rolling-induced extensive lamellar alignment along the RD (Fig. 1 *D*–*I* and *SI Appendix*, Fig. S6). Moreover, compared to as-cast lamellae, our partially recrystallized lamellae consisting of differently oriented and scaled (sub-) grains (Fig. 1 *E*–*G*) can better carry/coordinate plastic deformation; thereby alleviating/preventing stress concentrations and severe incompatible deformation between different lamellar regions.

Sustained High HDI Strain Hardening. To verify these salient improvements while offering more fundamental understandings, we next investigated the relevant multilength-scale deformation details and reinforcement mechanisms underlying our hierarchical HLS at different strain stages.

First, the very short annealing duration not only makes the processing cost-effective but also prevents excessive recrystallization, thus retaining these essential hetero-lamellae inherited by cold rolling, as revealed in Fig. 1 *D*–*I*. During tensile deformation, after two phases co-deform elastically, these soft FCC lamellae first begin to plastic deformation, as indicated by well-defined slip lines on the

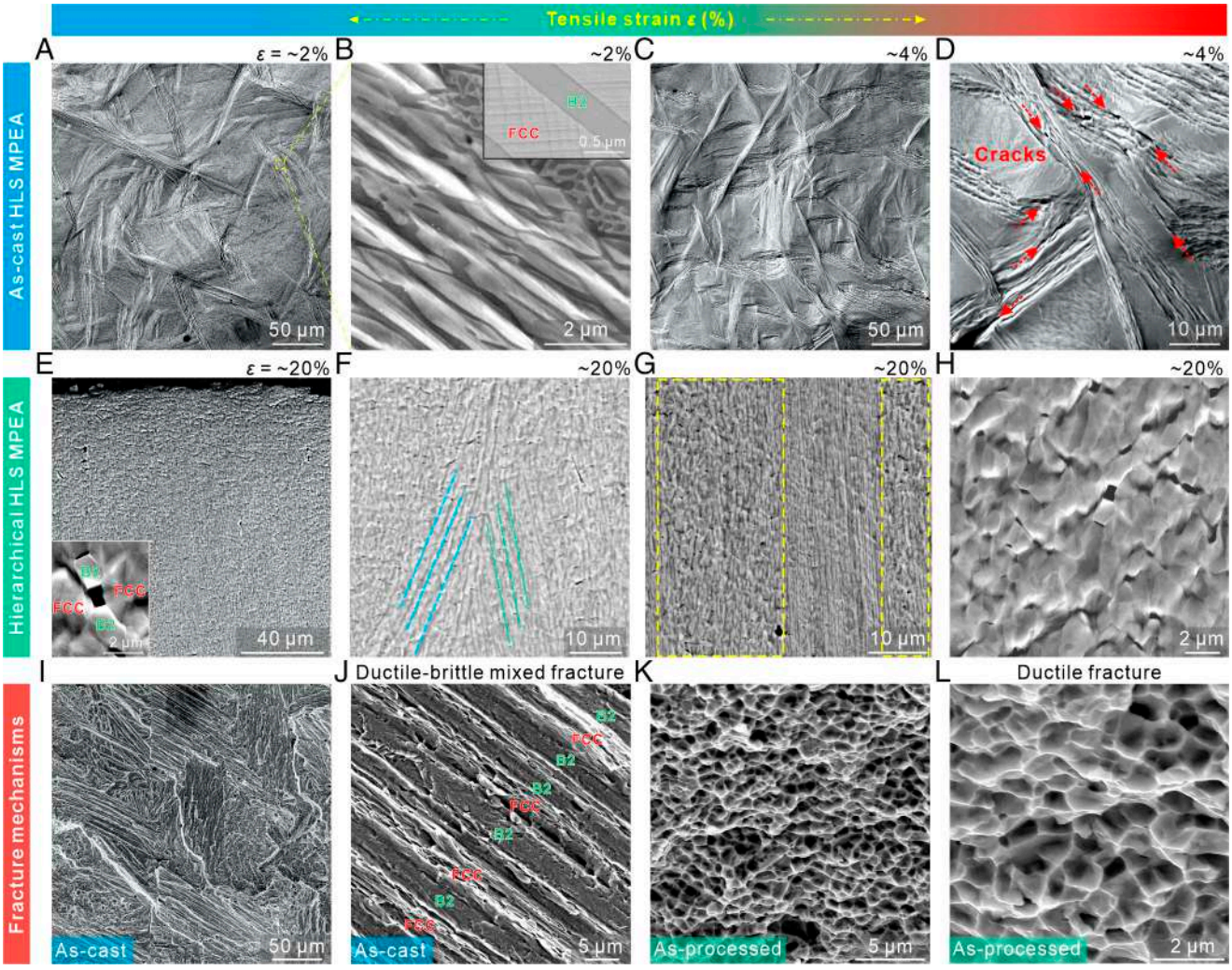

Fig. 3. Typical SEM images of different damage and failure mechanisms of as-cast and as-processed $Al_{0.7}CoCrFeNi$ MPEAs. (*A*–*D*) Gradually increased undulations on the prepolished surface of the as-cast MPEA. (*B*) Enlarged SEM image and its *Inset* revealing dense slip lines in the FCC phase. (*C*) Severe undulations on the prepolished surface. (*D*) SEM image revealing the initiated and extended cracks (marked by red arrows) at some stress concentration sites. (*E*–*H*) Microcrack distribution near the fractured end in the as-processed MPEA. These microcracks are mainly distributed in weak lamellar and nonlamellar regions (marked by yellow frames in *G*), whereby the incompatible deformation between hard brittle B2 grains triggers a grain-boundary cracking (*H* and *Inset* of *E*), as further evidenced by delicate STEM probing (Fig. 5*H*). (*F*) Relatively smaller angle (<30°) between two adjoining lamellar regions (marked by blue and green dotted lines). (*I*–*L*) Two types of fracture morphologies. (*J* and *L*) Enlarged SEM images revealing a ductile-brittle mixed fracture of the as-cast MPEA (*J*; see *SI Appendix, Note S6* for detailed fracture processes), and the distinct ductile fracture mode of the as-processed MPEA with massive dimples (*L*).

prepolished sample surface (see SEM *Inset*, Fig. 4*A*). Nevertheless, these soft FCC lamellae cannot plastically deform freely owing to the constraint by the still elastic B2 lamellae (14). Thus, these FCC lamellae appear much stronger than when they are not constrained, producing so-called synergetic strengthening as well as significantly elevating the yield strength of our HLS materials (4). In addition, considering the strain continuity, this implies the existence of plastic-strain gradients near these phase interfaces. To confirm that, we performed nanoscale TEM probing, revealing some parallel dislocations along the (111) primary slip plane accumulated in the FCC lamellae around phase interfaces (Fig. 4*A*). These dislocations, manifesting as an intense linear piling-up pattern, are known as geometrically necessary dislocations (GNDs), thus developing strain gradients as well as effectively coordinating the interphase hetero-deformation. As tensile strains increase, more pronounced slip-lines activities are observed (*SI Appendix*, Fig. S8), where the underlying GND-coordinated hetero-deformation (Fig. 4 *B*–*D*) hence will produce back stress in the opposite direction of the applied shear stress, thereby strengthening and strain-hardening these FCC lamellae. In turn, the back stress will induce a forward stress in the adjacent hard B2 phase to promote its plastic deformation (26, 31). Such that strong HDI stress and enhanced strain hardening can be established around hetero-lamellar zones due to the kinematic interplay between the two kinds of stresses during tension (31).

With increasing tensile strains, we also detected abundant SFs, Lomer–Cottrell (L-C) locks, and even nanotwinning (see Fig. 5 *A*–*C* and their *Insets*). Note that such a high density of 2D defects is quite unexpected, under the current quasi-static tensile condition, in this studied MPEA; because their extensive activation, especially deformation twinning (19, 32), requires ultrahigh strain rates of $>=10^2$ S^{-1} rather than the current ~10^{-3} S^{-1}. To unveil the physical origin

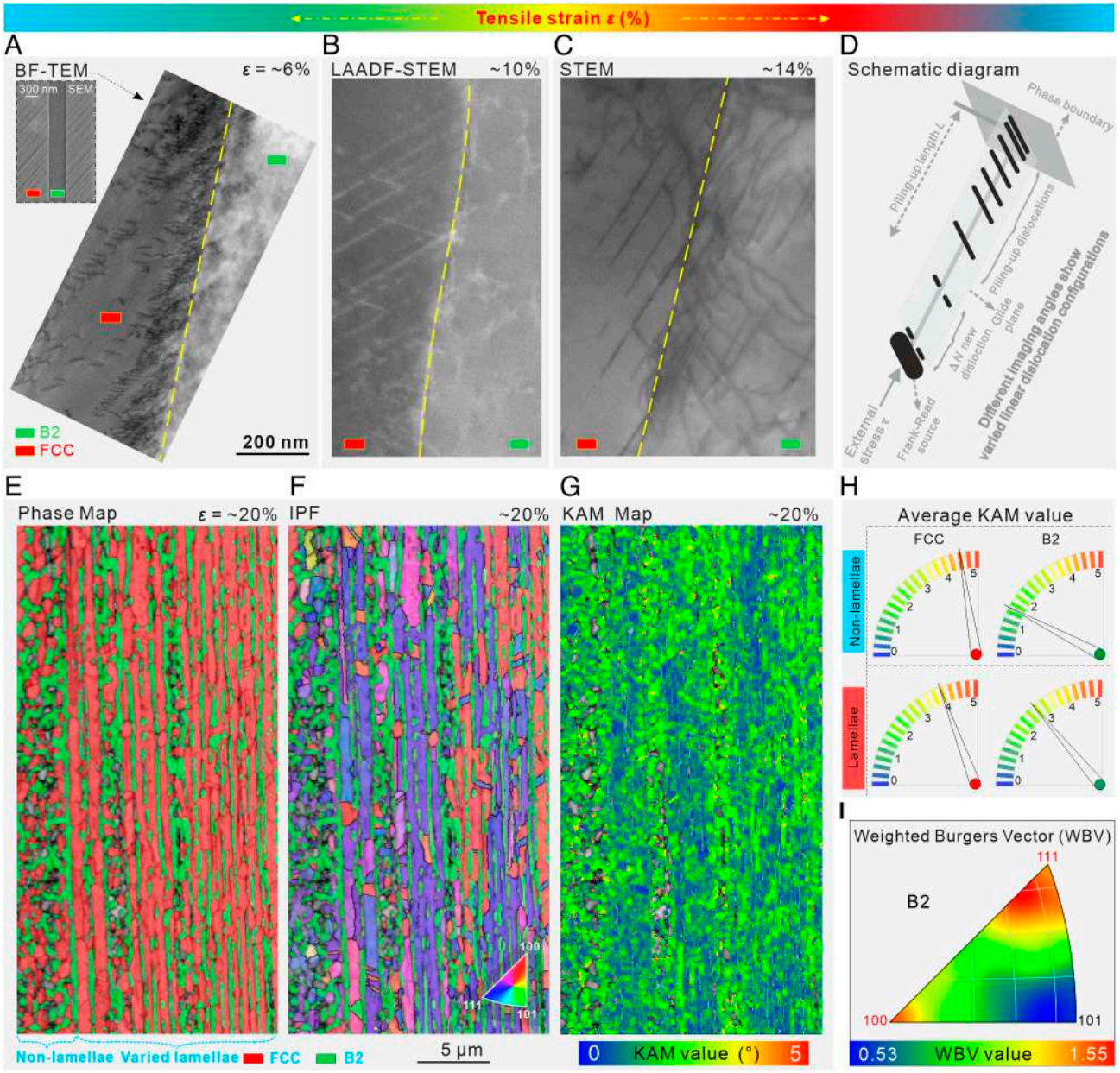

Fig. 4. (*A*–*D*) Intense, increasing dislocation piling-ups and (*E*–*G*) multiscale, topologically varied hetero-deformation of different feature regions in as-processed hierarchical HLS MPEAs. (*A*–*C*) TEM, LAADF-STEM, and bright-field STEM images, respectively. The SEM *Inset* (*A*) shows well-defined slip lines of the FCC phase on the prepolished sample surface. (*D*) Schematic diagram illustrating that different configurations of dislocation piling-ups can emerge, as indicated in (*A*–*C*), when being observed at different imaging angles (i.e., gradually departing from the $[110]_{FCC}$) in order to better reveal the defect evolution of adjoining B2 phase. (*E*–*I*) Multiple and quantitative EBSD characterizations.

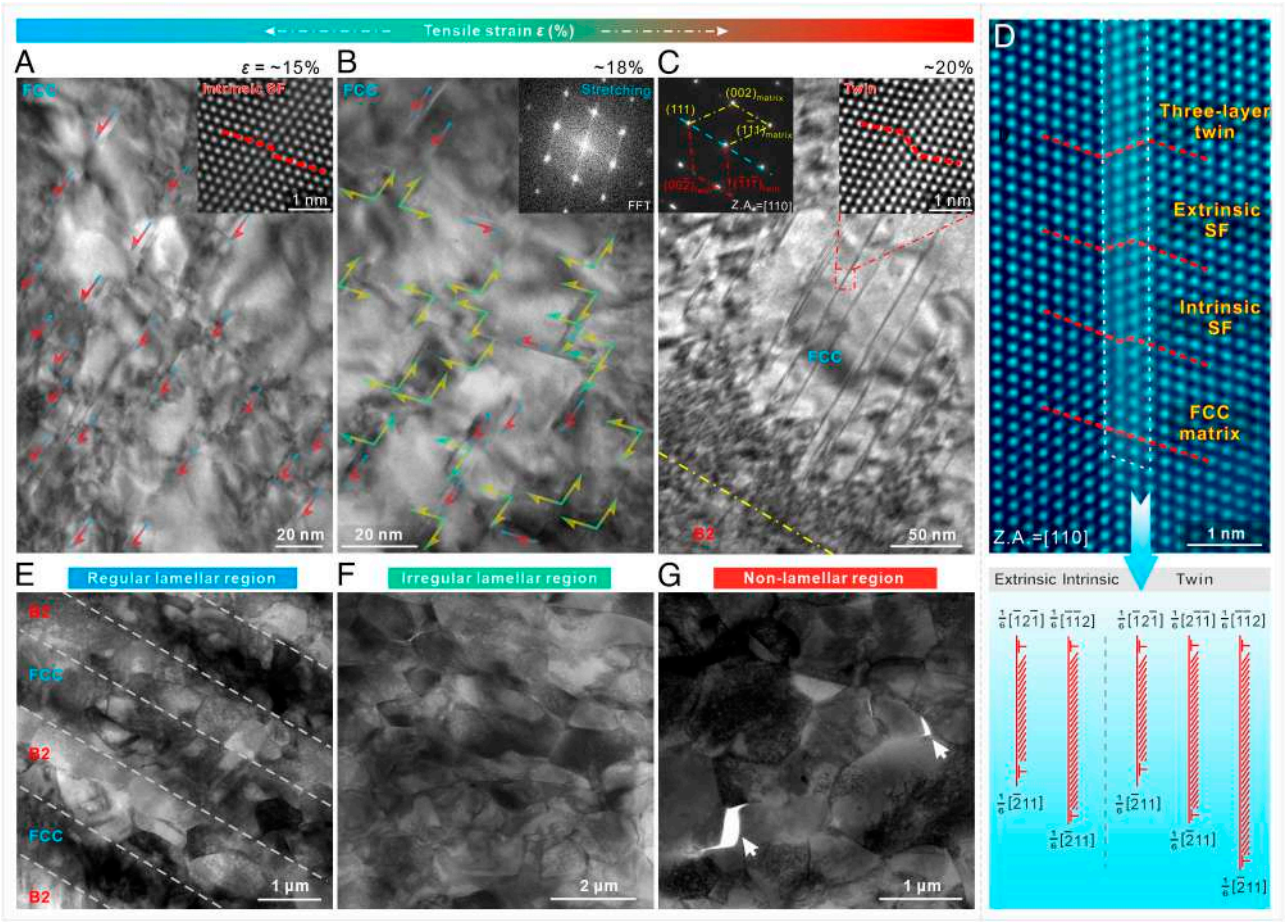

Fig. 5. Multiple and multiscale TEM characterizations of SFs (*A*), L-C locks (*B*), and nanotwins (*C* and *D*) as well as dual-phase deformation in different regions (*E*–*G*) in our hierarchical HLS MPEAs. (*A* and *B*) SFs and L-C locks marked by single and intersecting arrows, respectively. (*A*–*C*) Four *Insets* showing atomic-resolution STEM image of SF, fast Fourier transform (FFT) image of L-C locks, SAED pattern of twins and atomic-resolution STEM image of nanotwinning, respectively. (*D*) Twinning mechanism revealed by atomic-resolution STEM imaging and schematic diagram. (*E*–*G*) STEM images revealing significant plastic deformation of both FCC and B2 phases (*E* and *F*), while the limited plastic deformation of the B2 phase with poor dislocation storage (*G*) causes incompatible deformation between B2 grains, thereby leading to the grain-boundary cracking (marked by white arrows).

of this atypical deformation, we performed first principle density functional theory (DFT) calculations using the Vienna ab initio simulation package (*SI Appendix*, *Note S3*), whereby the SF energy (SFE) of our FCC phase is estimated on the basis of its chemical composition (Fig. 6*A*). For comparison, we also estimated the SFEs of two equiatomic FCC-structured CoCrNi and VCoNi medium-entropy alloys using the same method (Fig. 6*B*). As widely reported, the CoCrNi is readily subject to twinning deformation, while the VCoNi is prone to dislocation slip, due to low and high SFEs, respectively (6, 33–35). Here, our calculated average stable SFE values for CoCrNi and VCoNi alloys are −34 mJ/m^2 and 9 mJ/m^2, respectively, while the average SFE for our FCC phase is 3 mJ/m^2 (Fig. 6*C*). As such, our FCC phase, displaying a comparable SFE level as the VCoNi alloy, should prevail a dislocation-mediated deformation mechanism with a rather low possibility for twinning deformation. Thus, the abnormal twinning incident in our HLS MPEAs can be ascribed to the established strong HDI stress, which is enough large so that reaches the ultrahigh activation stress of twinning for our FCC phase, as further illustrated in *SI Appendix*, *Note S4*. In turn, this anomaly conveys an important and general lesson: Materials with high SFEs can be remodeled for the activation of deformation twinning and its exploitation for strengthening, if the required high stress intensities can be achieved by other mechanisms, such as the current HDI stress.

Our work thus revises the common understanding that deformation twinning is inaccessible in high SFE materials under quasi-static loading conditions, by showing that twinning can be triggered as a regular bulk deformation mechanism when the activation stresses for competing deformation mechanisms (usually dislocation motion) are high enough yet without reaching the fracture stress. Thus, applying a higher strain rate (>1 × 10^{-2} s^{-1}) is expected to trigger denser stacking faults and nanotwinning, as well as facilitate more extensive dynamic interactions among themselves and with lattice dislocations, thereby leading to further strength–ductility enhancement (32).

To resolve atomic-scale details, delicate STEM characterizations were applied to reveal the associated twinning mechanism, see Fig. 5*D*. Similar to that proposed by Mahajan and Chin (36), the detected extrinsic-intrinsic SF pair serves as an intermediate step preceding the formation of three-layer twin embryo, as further shown in the schematic diagram (Fig. 5*D*). This twinning mechanism is distinctly different from the classic pole mechanism for twinning widely detected in low-SFE MPEAs (37), in which one partial dislocation forms a whole twin via climbing a screw dislocation pole to adjacent slip planes. This mechanism comparison further validates the prevailing nature of strong HDI stress, which, under the present unfavorable SFE condition, activated the twinning deformation with an atypical formation mechanism. Eventually, the activated nanotwinning assisted with abundant SFs enhances plastic deformability and benefits additional strain hardening, alleviating stress concentrations around profuse hetero-lamellar zones.

In addition, large-area EBSD probing (Fig. 4 *E*–*G*) was also conducted, revealing that the FCC phase of these lamellar regions

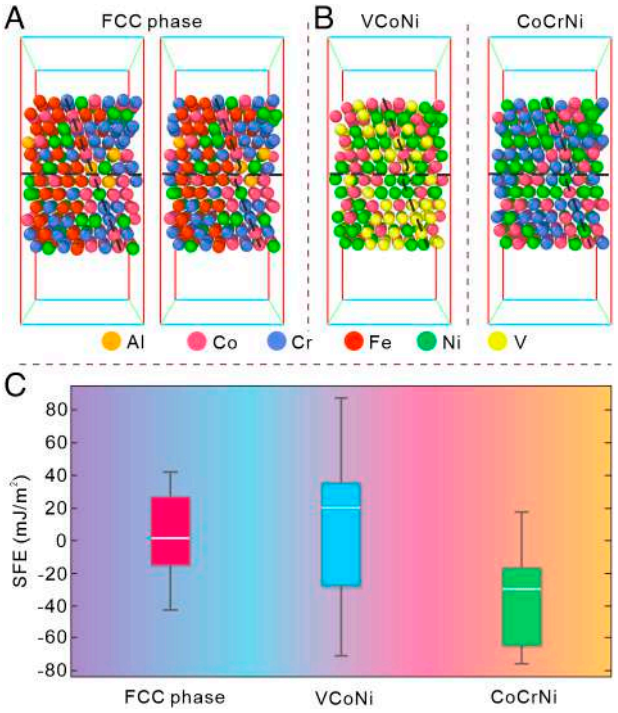

Fig. 6. DFT calculations of the stacking fault energy. (*A*) Optimized original FCC structure and the shifted structure with an intrinsic stacking fault for the FCC phase of our studied $Al_{0.7}$CoCrFeNi MPEA. 288 atoms are included in the supercell. (*B*) Optimized FCC structure with an intrinsic stacking fault for VCoNi and CoCrNi. (*C*) Distribution of calculated stacking faults energies for the FCC phase of our studied $Al_{0.7}$CoCrFeNi MPEA, VCoNi, and CoCrNi. The FCC phase is one of the two phases in our studied $Al_{0.7}$CoCrFeNi MPEA, and both VCoNi and CoCrNi MPEAs have a single FCC structure.

shows broadly varying Kernal average misorientation (KAM) values. This KAM trend can be ascribed to the topologically varied lamellar continuity (Fig. 4*G*), which renders different deformation constraining intensities within these lamellar regions (14). Thus, high KAM-value variations are observed between these lamellar and nonlamellar regions. Specifically, because of strong constraining deformation by the B2 phase, the FCC phase in these lamellar regions exhibits a lower KAM value of ~3.97°, while the weakened constraint in a few nonlamellar regions renders the FCC phase with a higher KAM value of ~4.46° (Fig. 4*H*). The ensuing severe plastic deformation in the latter even causes some FCC-phase components to be not fully resolved in our EBSD characterizations (Fig. 4 *E*–*G*).

Also, these above cases qualitatively explain that due to weak deformation constraining, many reported homogeneous-structured $Al_{0.7}$CoCrFeNi MPEAs (18–20, 38) exhibit lower yield strength (650 to 900 MPa) than our gigapascal-level hierarchical HLS samples (Fig. 2*C*), even if some of them possess comparable grain sizes. Meanwhile, it is reasonably deduced that these higher-strength lamellar regions in our HLS can also constrain the deformation of adjoining nonlamellar regions to a certain degree (39), considering that the latter are fully embedded in extensive lamellar regions, as revealed in Figs. 1*D* and 4 *E*–*G* and *SI Appendix*, Fig. S6. Thus, operating between the B2 and FCC phases as well as lamellar and nonlamellar regions, these multiple, multiscale constraint effects contribute to the observed high yield strength in Fig. 2*E*. Hence, it can be further concluded that a progressive hetero-deformation is developed in our designed hierarchical HLS, spanning from a few nonlamellar regions to extensive and diversified lamellar regions (with broadly varied lamellar length, thickness, and continuity). In addition, it is believed that different lamellar directions between some adjacent regions can also benefit the progressive hetero-deformation. Such that a sustained high HDI strain hardening underlying the multiscale progressive hetero-deformation can be achieved that promotes superior mechanical properties in Fig. 2 *C*–*E*.

Quantitative Loading-Unloading-Reloading (LUR), EBSD, and SHE-XRD Probing

To confirm and quantitatively demonstrate the sustainable HDI strain hardening, we conducted LUR experiments to measure the evolution of the HDI stress (Fig. 7 *A* and *B*). It was revealed that the HDI stress (~610 MPa) near the yield point was obviously higher than the effective stress in our hierarchical HLS-reinforced MPEAs. This stress trend quantitatively indicates the prevailing deformation constraining effect as revealed in our prior microstructure observations (Fig. 4 *E*–*G*), as well as explains that the larger HDI stress is responsible for the observed high yield strength (Fig. 2*E*). Here, of particular note is that the HDI stress increases continuously with increasing tensile strains (Fig. 7*B*). This is distinctly different from those reported evolution trends: Although many heterostructures readily produce the HDI stress that is much higher than effective stress, the former is prone to saturation during tensile deformation, especially at the later strain stage (14, 31, 39). This saturation manifests itself as a weakening of the HDI strain hardening. Thus, those reported conventional simple heterostructures often fail to improve ductility dramatically. However, as revealed in Fig. 7*B*, our hierarchical HLS design renders a continuous increase of the HDI stress, thus sustaining high HDI strain hardening. In sum, these LUR-evaluated results not only confirm our microstructure observations but also quantitatively reveal the high steady HDI hardening as the underpinning mechanism for the observed superior mechanical properties in Fig. 2 *C*–*E*.

Furthermore, we conducted in situ high-energy XRD experiments, revealing that the progressive, multiscale hetero-deformation promotes the continuous increase of dislocation density in the FCC phase (*SI Appendix*, Fig. S9). We did not detect the obvious saturation behavior of dislocations, which is often found in conventional hetero-structured materials (14, 31), indicative of the weakening of HDI hardening. This often saturation is due to the dynamic balance of dislocation multiplication and annihilation, especially at the later strain stage. Our unusual dislocation behavior may be ascribed to the extensive SF and nanotwinning activities as well as their intensive interactions in the FCC phase, which develop dense L-C locks and even manifest as interlocking defect networks (Fig. 5 *A*–*D*). These dynamic deformation incidents hence effectively suppress both dislocation recovery and annihilation (6, 7, 9). On the other hand, as these SFs, twins, L-C locks, and defect networks are generated dynamically, our hierarchical HLS tends to become more heterogeneous, thereby leading to intensified inhomogeneous plastic deformation (6). Such scenarios hence develop a dynamically reinforced HLS—which is naturally concomitant with more GND trapping—rationalizing the SHE-XRD-identified continuous dislocation increase (*SI Appendix*, Fig. S9). Thus, along with the persistent accumulation and proliferation of dislocations, the sustainable HDI strain hardening underlying our dynamically reinforced HLS gives rise to these record-high property combinations (Fig. 2 *C*–*E*).

Next, we focused on the deformation mechanism of the B2 phase in our hierarchical HLS. As per discussion above, due to intense stress interactions, the back stress accumulated in the FCC phase will induce a high forward stress into the adjacent B2 phase, thus activating its plastic deformation (14). Here, we indeed observed that under strong forward stress, these phase interfaces, acting as dislocation sources, emit abundant dislocations into the B2 phase with increasing strains, as revealed by joint low-angle annular dark-field (LAADF) STEM and direct STEM probing (Fig. 4 *B* and *C*). Moreover, the EBSD-assisted defect vector evaluation identifies these prevalent dislocations in the

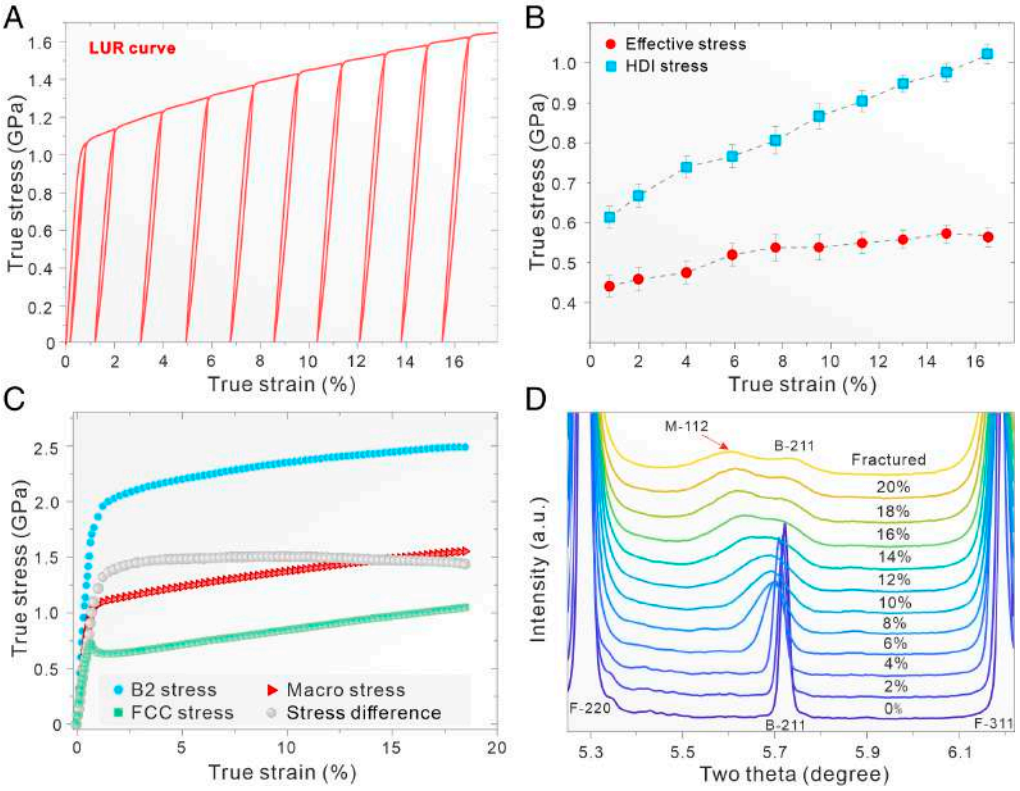

Fig. 7. Quantitative evaluations by LUR and SHE-XRD analysis. (*A*) LUR curve and (*B*) associated evolutions of the HDI stress and effective stress. (*C*) Stress-partitioning curves of the B2 and FCC phases evaluated by SHE-XRD, and stress–difference curve between B2 and FCC stresses. (*D*) In situ SHE-XRD patterns revealing the distinct martensite phase transformation. In (*D*), B, F, and M refer to B2 and FCC and martensite phases, respectively.

B2 phase dominated by the <111> Burgers vector (Fig. 4*I*). These <111>-type dislocations contain efficient 12 ISSs, thereby in favor of extensive plastic deformation, as mentioned above. Thus, at a fundamental level, it was confirmed that the B2 phase has contributed considerably to tensile deformation. This scenario differs obviously from the reported dislocation-density-limited plastic deformation of the B2 phase in $Al_{0.7}$CoCrFeNi MPEAs (18–20) and, in turn, rationalizes the observed excellent ductility in our hierarchical HLS MPEAs. In addition, this unusual deformation also implies that the established forward stress is rather high; otherwise, as discussed above, these efficient <111> dislocations cannot be activated successfully. Further EBSD analysis was applied to the B2 phase, revealing that it has a higher KAM value (~2.84°) in widespread lamellar regions compared to that in nonlamellar regions (Fig. 4*H*). This fact quantitatively indicates that the inherited hetero-lamellar architecture can significantly promote the plastic deformation of the hard B2 phase, because of rigid deformation constraints and thus the establishment of high forward stress. In contrast, in nonlamellar regions, the soft FCC phase experiences larger plastic deformation, because of not undergoing full deformation constraints (40). Thus, the relevant B2 phase under weaker forward stress exhibits a lower KAM value of ~1.46° (Fig. 4*H*).

Further SHE-XRD studies were conducted to resolve the in situ stress-partitioning evolution between the B2 and FCC phases. Such that we can simultaneously and quantitatively investigate the deformation behaviors of two phases throughout tensile deformation. It was revealed that the hard B2 phase exhibits a much higher yield strength of ~1.9 GPa, approximately threefold that of the soft FCC phase (Fig. 7*C*). Besides, it was detected that the strengths of both FCC (σ_{FCC}) and B2 (σ_{B2}) phases increase continuously with increasing strains, whereby the strength difference (i.e., $\sigma = \sigma_{B2} - \sigma_{FCC}$) basically remains constant throughout tensile deformation (Fig. 7*C*). Such a stress evolution revealed by SHE-XRD again supports our microstructure observations: Along with abundant SFs, L-C locks, and nanotwins (Fig. 5 *A*–*D*), the resultant progressive, dynamically reinforcing hetero-deformation across both different phases and regions is believed to greatly boost the successive stress increase in the FCC phase. Meanwhile, the intensive dislocation accumulation and multiplication in both FCC and B2 phases are also responsible for the continuous stress increase (Fig. 4).

Besides, high-energy XRD detected a minor martensite phase transformation in the B2 phase (marked by red arrow; Fig. 7*D* and *SI Appendix*, Fig. S10) of $Al_{0.7}$CoCrFeNi MPEAs. This phase-transformation incident hence sustains plastic deformation and supplements additional strain-hardenability at the later strain stage. On the other hand, this unique phase transformation also contributes to the stress increase of the B2 phase (Fig. 7*C*). Meanwhile, this incident experimentally demonstrates that the established forward stress in the B2 phase is very large, which not only enables extensive <111> dislocations but also activates phase transition. Such that the constant large strength difference between the FCC and B2 phases renders a sustained high HDI strain hardening, being consistent with prior LUR result (Fig. 7*B*).

In a nutshell, these SHE-XRD-resolved in situ, quantitative results greatly reinforce our understandings for strong HDI internal stress, especially these previously inaccessible benefits revealed in Figs. 4, 5 *A*–*E*, and 7, illuminating more fundamental strengthening and strain-hardening mechanisms lying behind our designed hierarchical HLS.

Extrinsic Ductilization Effect

We also investigated the damage-evolution mechanism of our hierarchical HLS MPEAs. There are extensive microcracks near the fractured end (Fig. 3*E* and *SI Appendix*, Fig. S11), instead of large (secondary) cracks usually seen in most literature reports. These microcracks are mostly distributed in the B2 phase (see *Inset*, Fig. 3 *E* and *H*) and exhibit complex varied morphologies, including circle-like, tortuous, and even a few submicron cracks (Fig. 3 *F*–*H*). In addition, there displays a markedly increased microcrack distribution from the regular lamellar regions, weak lamellar regions to nonlamellar regions (Fig. 3*G* and *SI Appendix*, Fig. S11). Many regular lamellar regions even only exhibit sporadic microcracks, thanks to intense

dual-phase hetero-deformation and strong HDI stress that make the B2 phase undergo substantial plastic deformation. In comparison, microcracks broadly occur in the weak lamellar and nonlamellar regions, especially the latter, due to the limited plastic deformation of the B2 phase. Also note that, in these regions, the formation of large cracks by the coalescence of small microcracks was generally inhibited, even when some of the microcracks are separated by only a single FCC phase (Fig. 3*H* and *SI Appendix*, Fig. S12). Moreover, it was revealed that these lamellar regions with strong dual-phase hetero-deformation can substantially suppress the growth/propagation of some relatively large and long cracks intruding from adjoining weak and nonlamellar regions (Fig. 3*G* and *SI Appendix*, Fig. S11).

This multiple and multiscale crack buffering effect hence prevents premature material failure, and instead, these cracks effectively supplement the strain to sustain and confer larger tensile deformation. To elucidate this salient crack buffering at the nanoscale, further microstructure observations are conducted by delicate STEM probing (Fig. 5 *E*–*G*). It was revealed that in regular and irregular lamellar regions, both FCC and B2 phases display significant plastic deformation with profuse dislocation storage (Fig. 5 *E* and *F*). In contrast, in nonlamellar regions, some B2-phase components exhibit poor dislocation accumulations (due to the general absence of deformation confinement), thereby leading to the observed grain-boundary cracking around them (marked by white arrows; Fig. 5*G*). But these ductile components of both FCC phase and lamellar regions can function as very efficient crack arresters and plastic buffering zones to hamper crack propagation and coalescence during tensile deformation (Fig. 3 *E*–*H* and *SI Appendix*, Figs. S11 and S12). Eventually, this intense crack buffering effect delays the onset of global damage, prolonging the intrinsic HDI and other strain-hardening mechanisms as well as delivering additional ductility.

Alternative Proof-of-Principle Demonstration

Finally, a critical and straightforward corroboration to the effectiveness of our design strategy is presented. After optimizing the processing route A to repeat/enhance the multiscale heredity-derived and -refined strategy (i.e., adopting the route B of *SI Appendix*, Fig. S13), a more remarkable property enhancement is achieved in Fig. 2*E* (see blue curve). Compared to our as-cast and the reported state-of-the-art properties, the uniform elongation, up to 26.5 ± 1.3%, significantly increases to over 2 and 5 times, respectively, yet without compromising yield strength. Such that the strength–ductility combination is further amplified in Fig. 2 *C* and *D*. The markedly enhanced elongation can be ascribed to the formation of more profuse and regular lamellar regions (*SI Appendix*, Fig. S14) compared to that processed by the route A. The increased lamellar regions may result from the stepwise elongation of some nonlamellar phase components during the second rolling, in favor of higher HDI strengthening and strain hardening. Corresponding LUR confirmation is provided in *SI Appendix*, Fig. S15. Besides, we have further applied our design strategy to an $AlCrFe_2Ni_2$ MPEA (*SI Appendix*, Figs. S16 and S17 and *Note S5*), which also promotes signification property enhancement (*SI Appendix*, Fig. S18).

Concluding Remarks

Our work presents a microstructural inheritance and refinement coupled multiscale design strategy, realized by fast and simple thermomechanical processing, yet creating superior and record-high strength–ductility combinations. In the designed hierarchical HLS, a progressive dual-phase hetero-deformation spanning across multiple length scales is sequentially activated from a few nonlamellar regions to extensive and diversified lamellar regions. Together with dynamically reinforcing hetero-deformation via SFs, L-C locks, nanotwins, and phase transformations, exceptionally sustainable HDI strengthening and strain hardening are achieved, thereby significantly improving both strength and ductility. Furthermore, an intense crack buffering effect (i.e., extrinsic ductilization mechanism) is triggered, which effectively prevents the previously reported premature failure and well stabilizes/prolongs the intrinsic HDI reinforcement mechanism. These sequentially activated multiscale hetero-deformations as well as complementary intrinsic and extrinsic reinforcement mechanisms are quite unexpected, yet absolutely essential, in light of the present tremendous strength–ductility enhancement, which are schematically illustrated in *SI Appendix*, Fig. S19. In sum, our demonstrated design strategy not only offers promising guidance for designing hierarchical heterostructured materials but also delivers many practical merits in guiding a broader group of advanced, cost-effective alloy development with strong-yet-ductile bulk properties. Furthermore, our rapid, economic design strategy, capable of extreme property enhancement, is of great economic, fundamental, and technological importance for many practical engineering applications.

Materials and Methods

Sample Preparation. Alloy ingots with a nominal composition of $Al_{0.7}CoCrFeNi$ (at%) were prepared by arc-melting a mixture of pure metals (purity >99.9 wt%). The ingots were remelted at least five times to achieve good chemical homogeneity in a copper mold of 40 mm (width) × 40 mm (length) × 12 mm (thickness). Subsequent processing routes are as follows:

Route A. Small pieces [40 mm (length) × 40 mm (width) × 2.1 mm (thickness)] were extracted from as-cast ingots and subjected to multipass cold-rolling to ~67% reduction in thickness using a laboratory-scale two-high rolling machine. The cold-rolled sheets were annealed at 1,000 °C for 10 min and then quenched in water immediately.

Route B. Small pieces were extracted from as-cast ingots and subjected to multipass cold-rolling (~50%). The cold-rolled sheets were annealed at 1,000 °C for 10 min and then water quenched, followed by cold rolling again (~67%). Subsequently, second annealing is conducted at 1,000 °C for 10 min and then water quenched immediately.

SEM, EBSD, TEM, STEM, LAADF-STEM, and HAADF-STEM Characterizations. The microstructure was characterized by a field-emission scanning electron microscope (Zeiss Gemini 360) EBSD characterizations were carried by a Symmetry S2 EBSD detector. Associated EBSD analysis was conducted by Oxford AZtecCrystal software. TEM, STEM, and HAADF-STEM analyses were conducted on JEOL-2100F and JEM-F200 TEM operating at 200 to 300 kV. Ultrahigh-resolution HAADF-STEM probing was examined using a probe Cs-corrected transmission electron microscope (JEM-ARM300F). These samples for SEM and EBSD investigation were prepared by standard metallographic polishing, followed by electropolishing using a mixture of 90% ethanol and 10% perchloric acid (vol%) at −30 °C. The mixture, combined with twin-jet electropolishing, is also used to prepare TEM specimens. Some methods of microstructure characterizations refer to ref. 40.

3D APT. The near-atomic-scale elemental information was gathered using a LEAP™ 5000X HR (CAMECA) under a high vacuum of 2×10^{-11} Torr. The APT results were reconstructed and analyzed employing the CAMECA integrated visualization and analysis software (IVAS 3.8.6). Needle-shaped samples for APT characterizations were prepared using the focused ion beam, see ref. 40.

Quasi-Static Tension and LUR Testing. Dog bone-shaped tensile samples with a gauge size of 13 × 3.0 × 0.65 mm^2 were cut from these prepared samples by wire electrodischarge machining parallel to the rolling direction. Tension was conducted in an MTS Exceed E44 machine with an initial strain rate of ~1×10^{-3} s^{-1}. To obtain a reproducible state, all tensile tests were repeated five times at least, using a 10-mm extensometer to monitor the strain. The same samples and equipment were used for LUR tests, see refs. 40 and 41 for the corresponding method.

Synchrotron-Based High-Energy XRD. In situ high-energy XRD measurements were carried out on the beam-line 11-ID-C, at the Advanced Photon Source, Argonne National Laboratory (APS, ANL), USA. During tensile loading, a monochromatic X-ray beam with energy ~105 keV (λ = 0.1173 Å) and beam size of 200 μm (height) × 200 μm (width) was used. A 2-D detector was placed ~1.70 m behind the tensile sample to record the scattering intensity. These calculation details about the dislocation density and phase-stress partitioning were discussed in *SI Appendix, Note S7*.

Data, Materials, and Software Availability. All study data are included in the article and/or *SI Appendix*.

ACKNOWLEDGMENTS. Y. Zhu is grateful for financial support from the National Key R&D Program of China (2021YFA1200202). Y. Zhong is grateful for financial support from the National Natural Science Foundation of China (No. U23A20607). Use of the Advanced Photon Source was supported by the U.S. Department of Energy, Office of Science, Office of Basic Energy Science, under Contract No. DE-AC02-06CH11357.

Author affiliations: [a]State Key Laboratory of Advanced Special Steel, Shanghai Key Laboratory of Advanced Ferromletallurgy, School of Materials Science and Engineering, Shanghai University, Shanghai 200444, China; [b]Department of Materials Science and Engineering, Hong Kong Institute for Advanced Study, City University of Hong Kong, Hong Kong, China; [c]Institute of High Performance Computing, Agency for Science, Technology and Research, Singapore City 138632, Singapore; [d]Department of Information and Computing Sciences, School of Mathematical Science, Peking University, Beijing 100091, China; [e]AI for Science Institute, Beijing 100085, China; [f]Department of Mechanical Engineering, The University of Hong Kong, Hong Kong, China; [g]Department of Advanced Design and Systems Engineering, City University of Hong Kong, Hong Kong, China; [h]Department of Mechanical and Aerospace Engineering, Hong Kong University of Science and Technology, Hong Kong, China; [i]Department of Physics, City University of Hong Kong, Hong Kong, China; and [j]Mechano-X Institute, Applied Mechanics Laboratory, Department of Engineering Mechanics, Tsinghua University, Beijing 100084, China

Author contributions: P.S. designed research; P.S., Y. Li, X.J., J.Y., R.Z., Y.Q., Y. Lin, J.H., B.T., Y.W., T.W., B.Y., C.L., J.L., Z.S., B.D., Q.L., T. Zheng, W.R., T. Zhang, Y.R., Y. Zhong, C.T.L., H.G., and Y. Zhu performed research; P.S., Z.L., J.Y., C.L., J.L., Y.R., Y. Zhong, C.T.L., H.G., and Y. Zhu contributed new reagents/analytic tools; P.S., Y. Li, Z.L., T. Zheng, Y.W., T.W., B.Y., W.R., T. Zhang, Y.R., Y. Zhong, C.T.L., H.G., and Y. Zhu analyzed data; and P.S., Y. Zhong, C.T.L., H.G., and Y. Zhu wrote the paper.

The authors declare no competing interest.

This article is a PNAS Direct Submission. P.K.L. is a guest editor invited by the Editorial Board.

1. J. W. Yeh *et al.*, Nanostructured high-entropy alloys with multiple principal elements: Novel alloy design concepts and outcomes. *Adv. Eng. Mater.* **6**, 299–303 (2004).
2. B. Chen *et al.*, Unusual activated processes controlling dislocation motion in body-centered-cubic high-entropy alloys. *Proc. Natl. Acad. Sci. U.S.A.* **117**, 16199–16206 (2020).
3. P. J. Shi *et al.*, Hierarchical crack buffering triples ductility in eutectic herringbone high-entropy alloys. *Science* **373**, 912–918 (2021).
4. X. Jiang *et al.*, Synergistic control of microstructures and properties in eutectic high-entropy alloys via directional solidification and strong magnetic field. *J. Mater. Res. Technol.* **28**, 4440–4462 (2024).
5. P. J. Shi *et al.*, Enhanced strength-ductility synergy in ultrafine-grained eutectic high-entropy alloys by inheriting microstructural lamellae. *Nat. Commun.* **10**, 489 (2019).
6. M. X. Yang *et al.*, Dynamically reinforced heterogeneous grain structure prolongs ductility in a medium-entropy alloy with gigapascal yield strength. *Proc. Natl. Acad. Sci. U.S.A.* **115**, 7224–7229 (2018).
7. B. Gludovatz *et al.*, A fracture-resistant high-entropy alloy for cryogenic applications. *Science* **345**, 1153–1158 (2014).
8. S. J. Chen *et al.*, Real-time observations of TRIP-induced ultrahigh strain hardening in a dual-phase CrMnFeCoNi high-entropy alloy. *Nat. Commun.* **11**, 826 (2020).
9. B. Gludovatz *et al.*, Exceptional damage-tolerance of a medium entropy alloy CrCoNi at cryogenic temperatures. *Nat. Commun.* **7**, 10602 (2016).
10. P. J. Shi *et al.*, A precipitate-free AlCoFeNi eutectic high-entropy alloy with strong strain hardening. *J. Mater. Sci. Technol.* **89**, 88–96 (2021).
11. Y. Li *et al.*, Unveiling microstructural origins of the balanced strength-ductility combination in eutectic high-entropy alloys at cryogenic temperatures. *Mater. Res. Lett.* **10**, 602–610 (2022).
12. J. Y. He *et al.*, Effects of Al addition on structural evolution and tensile properties of the FeCoNiCrMn high-entropy alloy system. *Acta Mater.* **62**, 105–113 (2014).
13. A. Asabre *et al.*, Influence of Mo/Cr ratio on the lamellar microstructure and mechanical properties of as-cast $Al_{0.75}$CoCrFeNi compositionally complex alloys. *J. Alloy Compd.* **899**, 163183 (2022).
14. P. J. Shi *et al.*, Strong-yet-ductile eutectic alloys employing cocoon-like nanometer-sized dislocation cells. *Adv. Mater.* **36**, 2405459 (2024).
15. P. Sathiyamoorthi, H. S. Kim, High-entropy alloys with heterogeneous microstructure: Processing and mechanical properties. *Prog. Mater. Sci.* **123**, 100709 (2022).
16. M. N. Hasan *et al.*, Simultaneously enhancing strength and ductility of a high-entropy alloy via gradient hierarchical microstructures. *Int. J. Plasticity* **123**, 178–195 (2019).
17. U. Hecht, S. Gein, O. Stryzhyboroda, E. Eshed, S. Osovski, The BCC–FCC phase transformation pathways and crystal orientation relationships in dual phase materials from Al-(Co)-Cr-Fe-Ni alloys. *Front. Mater.* **7**, 287 (2020).
18. B. Gwalani *et al.*, Influence of ordered $L1_2$ precipitation on strain-rate dependent mechanical behavior in a eutectic high entropy alloy. *Sci. Rep.* **9**, 6371 (2019).
19. B. Gwalani *et al.*, Dynamic shear deformation of a precipitation hardened $Al_{0.7}$CoCrFeNi eutectic high-entropy alloy using hat-shaped specimen geometry. *Entropy* **22**, 431 (2020).
20. Q. Wang *et al.*, On the room-temperature tensile deformation behavior of a cast dual-phase high-entropy alloy $CrFeCoNiAl_{0.7}$. *J. Mater. Sci. Technol.* **87**, 29–38 (2021).
21. Z. B. An *et al.*, Negative enthalpy alloys and local chemical ordering: A concept and route leading to synergy of strength and ductility. *Natl. Sci. Rev.* **11**, nwae026 (2024).
22. Z. B. An *et al.*, Negative mixing enthalpy solid solutions deliver high strength and ductility. *Nature* **625**, 697–702 (2024).
23. M. W. Wu *et al.*, Revealing the intensified preferred orientation and factors dominating the anisotropic mechanical properties of laser powder bed fusion Ti–6Al–4V alloy after heat treatment. *J. Alloy Compd.* **949**, 169494 (2023).
24. A. Ho *et al.*, On the origin of microstructural banding in Ti-6Al4V wire-arc based high deposition rate additive manufacturing. *Acta Mater.* **166**, 306–323 (2019).
25. L. Liu *et al.*, Loss-free tensile ductility of dual-structure titanium composites via an interdiffusion and self-organization strategy. *Proc. Natl. Acad. Sci. U.S.A.* **120**, e2302234120 (2023).
26. P. J. Shi *et al.*, Multistage work hardening assisted by multi-type twinning in ultrafine-grained heterostructural eutectic high-entropy alloys. *Mater. Today* **41**, 62–71 (2020).
27. J. M. Park *et al.*, Ultra-strong and strain-hardenable ultrafine-grained medium-entropy alloy via enhanced grain-boundary strengthening. *Mater. Res. Lett.* **9**, 315–321 (2021).
28. J. Y. He *et al.*, A precipitation-hardened high-entropy alloy with outstanding tensile properties. *Acta Mater.* **102**, 187–196 (2016).
29. B. Xiao *et al.*, Ultrahigh intermediate-temperature strength and good tensile plasticity in chemically complex intermetallic alloys via lamellar architectures. *Acta Mater.* **262**, 119459 (2024).
30. E. P. George *et al.*, Ordered intermetallics. *Annu. Rev. Mater. Sci.* **24**, 409–451 (1994).
31. Y. T. Zhu, X. L. Wu, Perspective on hetero-deformation induced (HDI) hardening and back stress. *Mater. Res. Lett.* **7**, 393–398 (2019).
32. K. X. Cui, J. W. Qiao, P. K. Liaw, Y. Zhang, Data driving design of high-entropy alloys for lightweight and dynamic applications. *Sci. China Phys. Mech.* **67**, 227101 (2024).
33. J. Ding *et al.*, Tunable stacking fault energies by tailoring local chemical order in CrCoNi medium-entropy alloys. *Proc. Natl. Acad. Sci. U.S.A.* **115**, 8919–8924 (2018).
34. X. Bowen *et al.*, Harnessing instability for work hardening in multi-principal element alloys. *Nat. Mater.* **23**, 755–761 (2024).
35. L. Y. Zhu, Z. X. Wu, Effects of short range ordering on the generalized stacking fault energy and deformation mechanisms in FCC multiprincipal element alloys. *Acta Mater.* **259**, 119230 (2023).
36. S. Mahajan, G. Y. Chin, Formation of deformation twins in fcc crystals. *Acta Metall.* **21**, 1353–1363 (1973).
37. Y. T. Zhu, X. Z. Liao, X. L. Wu, Deformation twinning in nanocrystalline materials. *Prog. Mater Sci.* **57**, 1–62 (2012).
38. S. Gangireddy *et al.*, Contrasting mechanical behavior in precipitation hardenable Al_xCoCrFeNi high entropy alloy microstructures: Single phase FCC vs. dual phase FCC-BCC. *Mater. Sci. Eng. A* **739**, 158–166 (2019).
39. X. L. Wu *et al.*, Heterogeneous lamella structure unites ultrafine-grain strength with coarse-grain ductility. *Proc. Natl. Acad. Sci. U.S.A.* **112**, 14501–14505 (2015).
40. P. J. Shi *et al.*, Bioinspired, heredity-derived hierarchical bulk multifunctional copper alloys. *Mater. Today.* **71**, 22–37 (2023).
41. M. X. Yang *et al.*, Back stress strengthening and strain hardening in gradient structure. *Mater. Res. Lett.* **4**, 145–151 (2016).